GSA Data Repository 2019332

Harel et al., 2019, Drainage reversal toward cliffs induced by lateral lithologic differences

SUPPLEMENTARY TABLE, FIELD AREA DESCRIPTION, METHODS AND FIGURES

(1) Table DR1. List of channels that transect the Southwestern Arava escarpment

(2) Field area DR1.

(3) Methods DR1. Calculating the χ map, DEMs production using drone acquired aerial photos, defining the northing trend, measuring the apparent thickness of the erodible valley fill layer, automatic calculation of tributary junction angle.

(4) Figure DR1.

(5) Figure DR2.

(6) Figure DR3.

(7) Figure DR4.

(8) Figure DR5.

(9) Figure DR6.

(10) Figure DR7.

(11) Figure DR8.

(12) Figure DR9.

(13) References.

(1) TABLE DR1. LIST OF CHANNELS THAT TRANSECT THE SOUTHWESTERN ARAVA ESCARPMENT*

Index	Basin/ Windgap[‡‡]	Intersection with escarpment cliff: Lat.,lon.	Reversed length[**] [m] (±20)	Embayment length[#][m] (±20)	Windgap to waterfall Height difference [m] (±2)	Height of rock outcrop upstream from waterfall [m] (±2)	Apparent thickness of erodible fill[##] (±2) [m]	barbed tributaries angle[###]
1[†]	Ktura	35.06314/ 30.03613	4668	1149	32	5	27	152, 135, 143, 108, 105
2	Ktura	35.05994/ 30.02146	234	386	14	-	14	-
3[†]	Grofit	35.04618/ 30.01145	1827	1207	37	7	30	99, 99, 128, 150, 102
4	Grofit	35.05071/ 30.0049	172	534	12	-	12	-
5	Grofit	35.04444/ 29.99491	385	-	42	29	13	-
6[†]	Grofit	35.04107/ 29.99121	690	246	25	6	19	136
7[†]	Aya-Grofit	35.03804/ 29.98715	-	-	-	-	-	-
8[†]	Grofit	35.03658/ 29.98446	271	30	11	6	5	136
9[†]	Kasuy-Grofit	35.03461/ 29.98076	-	-	-	-	-	-
10[†,‡]	Itro east	35.03388/ 29.97235	443	118	29	6	23	110
11	Itro-Itro east	35.03228/ 29.96649	-	-	-	-	-	-
12	Itro-Itro east	35.03229/ 29.96442	-	-	-	-	-	-
13[†]	Itro-Itro east	35.02985/ 29.96066	-	-	-	-	-	-
14	Itro-Itro east	35.02917/ 29.9584	-	-	-	-	-	-

Index	Basin/ Windgap[‡‡]	Intersection with escarpment cliff: Lat.,lon.	Reversed length[**] [m] (±20)	Embayment length[#][m] (±20)	Windgap to waterfall Height difference [m] (±2)	Height of rock outcrop upstream from waterfall [m] (±2)	Apparent thickness of erodible fill[##] (±2) [m]	barbed tributaries angles[###]
15	Itro-Itro east	35.02891/ 29.95535	-	-	-	-	-	-
16	Itro-Itro east	35.02822/ 29.95353	-	-	-	-	-	-
17	Reuel east	35.02768/ 29.95075	98	84	8	-	8	-
18	Reuel east	35.02604/ 29.94773	123	-	11	-	11	-
19[†]	Itro-Reuel east	35.02308/ 29.94368	-	-	-	-	-	-
20[†]	Itro-Reuel east	35.02207/ 29.94307	-	-	-	-	-	-
21[†]	Itro-Reuel east	35.01993/ 29.94087	-	-	-	-	-	-
22[†]	Reuel east	35.01758/ 29.93996	79	-	6	3	3	-
23	Reuel east	35.01455/ 29.93656	23	-	3	-	3	-
24	Shaharut-Reuel east	35.0098/2 9.92917	-	-	-	-	-	-
25[†,‡]	Shaharut east	35.00787/ 29.91923	185	-	13	1	12	-
26	Shaharut-Shaharut east	35.00657/ 29.91491	-	-	-	-	-	-
27	Shaharut-Shaharut east	35.00574/ 29.91274	-	-	-	-	-	-
28	Shaharut-Shaharut east	35.00559/ 29.91139	-	-	-	-	-	-
29	Shaharut east	35.00477/ 29.90434	17	-	1	-	1	-
30†	Shaharut east	34.99676/ 29.90046	45	-	5	3	2	-

Index	Basin/ Windgap[*]	Intersection with escarpment cliff: Lat.,lon.	Reversed length[**] [m] (±20)	Embayment length[#][m] (±20)	Windgap to waterfall Height difference [m] (±2)	Height of rock outcrop upstream from waterfall [m] (±2)	Apparent thickness of erodible fill[##] (±2) [m]	barbed tributaries angles[###]
31[†]	Shaharut east	34.99412/ 29.89555	114	-	7	-	0[§]	-
32[†]	Yotvata	34.99477/ 29.88625	65	-	7	-	7	-
33	Tze'ela-Yotvata	34.98087/ 29.87275	-	-	-	-	-	-
34	Tze'ela-Yotvata	34.98024/ 29.87202	-	-	-	-	-	-
35	Argaman	34.9816/ 29.84957	80	-	5	-	5	-
36[†]	Kadkod	34.97173/ 29.84269	24	142	1	-	10[§§]	-
37	Uvda-Sasgon	34.96381/ 29.82544	-	-	-	-	-	-
38	Uvda-Sasgon	34.96188/ 29.82365	-	-	-	-	-	-

Notes:

*Our observations of the highland drainage network are based on morphometric analysis over a 12 m DEM acquired from TanDEM-X (Wessel, 2016).

[*]The basin name refers to the transect between the channel and the escarpment. In reversed channels, the transect is a waterfall, and the name represents the east draining basin. When there is no reversal, the transect is a saddle, and its name represents the two basins that diverge from it.

[**]Distance along flow from the windgap to the waterfall.

[#]Distance along flow from the waterfall to a line that represents the regional escarpment cliff.

[##] see methods DR1.

[###] see methods DR1.

† sites that were surveyed in the field.

‡Measured from a drone created DEM. Reported errors are smaller than TanDEM-X data: the horizontal error is 0.1m and the vertical error is 0.06m.

§ A field survey reveals that here, the reversed channel is not associated with incision into valley fill, but it was likely formed by a natural dam in the antecedent channel. More specifically, the windgap in this location is associated with coarse deposits at the outlet of a side tributary, these deposits are likely associated with debris flow deposits that dammed the channel and induced its reversal.

§§Nine meters of alluvial coating sitting on the waterfall.

(2) FIELD AREA DR1.

The Arava Valley is a rift like structure stretching between the Dead Sea and the Gulf of Aqaba, that is part of the transtensional Sinai-Arabia plate boundary. Several tectonic and structural features control the morphology of the Arava Valley: (1) A series of steep normal faults bound the Arava Valley from both the Jordanian heights in the east and the Israeli Negev in the west (Amit et al., 2002; Garfunkel et al., 2014). These faults contribute to its rift like morphology, with a 5-10 km wide valley bounded by high eastern shoulders and segmented lower western shoulders. (2) A segmented strike-slip system that induces the sinistral offset between the plates (Ginat et al., 1998; Garfunkel et al., 2014; Beyth et al., 2018). (3) Further to the west, extending sub-parallel to the Arava Valley, an asymmetrical wide anticline has been proposed to be reactivated in the Plio-Pleistocene (Wdowinski and Zilberman, 1996, 1997; Ginat et al., 2000) and to induce east or northeast tilt of the central and southeastern Negev toward the Arava Valley (Ginat et al., 2000).

In the current research, we focus on the escarpment segment that bounds the Southern Arava Valley from the west. Here, the escarpment is shoulder-type with a major water divide that mostly follows the escarpment cliff. To the east of the water divide, steep basins drain to the southern Arava, and to its west, low relief channels are incised into table-like interfluves and flow west to Biqa't Uvda, before joining the Hiyyon basin that drains to the central Arava Valley.

The current drainage configuration differs significantly from the drainage geometry of the previous geologic epochs (Avni et al., 2000). Prior to the formation of the Sinai-Arabia plate boundary, in the early Miocene (Garfunkel et al., 2014), large

rivers drained west from Arabia across the present day Arava Valley to the Mediterranean, over an extensive truncated surface that was formed in the Oligocene (Avni et al., 2012; Mart and Vachtman, 2015). In the Pliocene, segments of the central and southern Arava Valley have already formed, acting as local base levels. Nonetheless, other parts were less subdued, allowing a drainage regime whereby areas east to the Arava Valley were drained across the Sinai-Arabia plate boundary toward the central Negev. Finally, during the early quaternary, a major phase of drainage reorganization redirected large drainages of the southeastern Negev to the central Arava Valley by a series of capture events (Avni et al., 2000; Guralnik et al., 2010).

The climatic conditions are hyper-arid with precipitation rate $\lesssim$50 mm/yr. It was suggested that with the exception of relatively short-lived episodes of more humid conditions during the late Pliocene and Pleistocene (Beyth et al., 2018; Vaks et al., 2013), the current hyper-arid conditions have persisted since the late Pliocene (Vaks et al., 2013).

(3) METHODS DR1.

Method 1: **Calculating the χ map**

Figure 3 in the main text depicts a χ map of the study area and of the basins that drain the escarpment to the east. χ was calculated over the drainage network defined by using a threshold drainage area of 50 pixels (pixel dimensions are 30x30 m). χ was defined using the equation (Willett et al., 2014):

$$\chi(x)= \int_{x_b}^{x} \left(\frac{A_0}{A(x')}\right)^{\theta} dx'$$

with A_0= 1 m^2, θ = 0.3, which was found to linearize the main trunk and tributaries (Perron and Royden, 2012) of the largest basin, and x_b is set to be at elevations of 135 m.

Method 2: **Producing DEMs using drone acquired aerial photos and determining terrace extension**

We generated high resolution DEMs and orthophotos for channels 10 and 25 in table DR1 from aerial photos acquired by a DJI Phantom III drone with ~80% overlap between the photos. The DEMs and the orthophotos were produced using the Agisoft 'Photoscan' commercial code that applies a SfM algorithm. Differential GPS was used to accurately locate 20 anchoring points in each site. The longitudinal profiles of the active channels and the terraces (Fig. 3E and 3F) were extracted from the DEMs and validated against field mapping.

The horizontal extent of the terraces shown in Fig. DR8 was determined by a four steps procedure using ArcGIS: First, a slope raster was generated and a threshold slope (2^o in fig. A, 7^o in Fig B) was used to define pixels of low slope. Second, regions with high density of low-slope pixels were identified by dividing the region to coarser pixels (1 and

1.4m for fig. A and B respectively) and searching for the number of low-slope fine pixels within a 1m radius circle that was centered in each coarse pixel. Coarse pixels with low density of low slope fine pixels (<3.8% and <5.5%, in fig. A and B respectively) were eliminated. Third, the circumferences of areas with high density of coarse pixels that are not part of the channels were defined as terraces and mapped as polygons. Finally, the terrace polygons were validated against field mapping of terraces and final editing was performed.

In the upper Shaharut east basin, channel 25 in table DR1 (Fig. DR8A), the areas that were disturbed by a dirt road were eliminated from the terrace polygons. In the same site, the channel might also be disturbed by the dirt road, but the water divide and the waterfall locations and elevations are likely unaffected, so the road does not have a significant effect on the channel profile.

Method 3: **Defining the northing trend**

Figure 4B shows the length of the reversed channels as a function of a northing trend. Northing was defined based on the Euclidian distance to the southmost windgap, No. 38 in table DR1. Each channel is represented by its transect point with the cliff, which is either a waterfall or a saddle.

Method 4: **Measuring the apparent thickness of the erodible valley fill layer**

Column 8 in table DR1 reports the apparent thickness of the erodible fill unit into which the reversed channel incises. The apparent thickness was defined as the elevation difference between the windgap (which is consistently located on top of the erodible fill)

and the closest contact between the erodible fill and the underlying bedrock (Fig. DR7), which was typically at or slightly upstream from the lip of the waterfall. Bedrock exposure location was identified in the field, and by using field photos and orthophotos. Where we identified valley fill on the waterfall (no. 36 in table DR1), we added its thickness to the estimation of the apparent thickness. The true fill thickness (as opposed to the apparent thickness) is expected to be larger due to the westward grading of the antecedent channels. The estimation of the true thickness requires knowledge of the antecedent slope, which is rarely preserved.

Method 5: **Automatic calculation of tributary junction angle**

Column 9 in table DR1. reports the tributary junction angle for barbed tributaries. The junction angle was calculated automatically using a Matlab script. Upon manual selection of a tributary channel head and the tributary junction points, the script calculates the orientation of two lines. The lines are defined based on orthogonal linear regressions through the pixels of the drainage network. The first line uses the drainage network pixels between the two chosen points. The second line uses the pixels between the junction point and a point that is located upstream from it, at a distance which is half of the along flow length of the tributary. The junction angle is defined as the difference between the orientations of the two lines.

158 (4) FIGURE DR1.

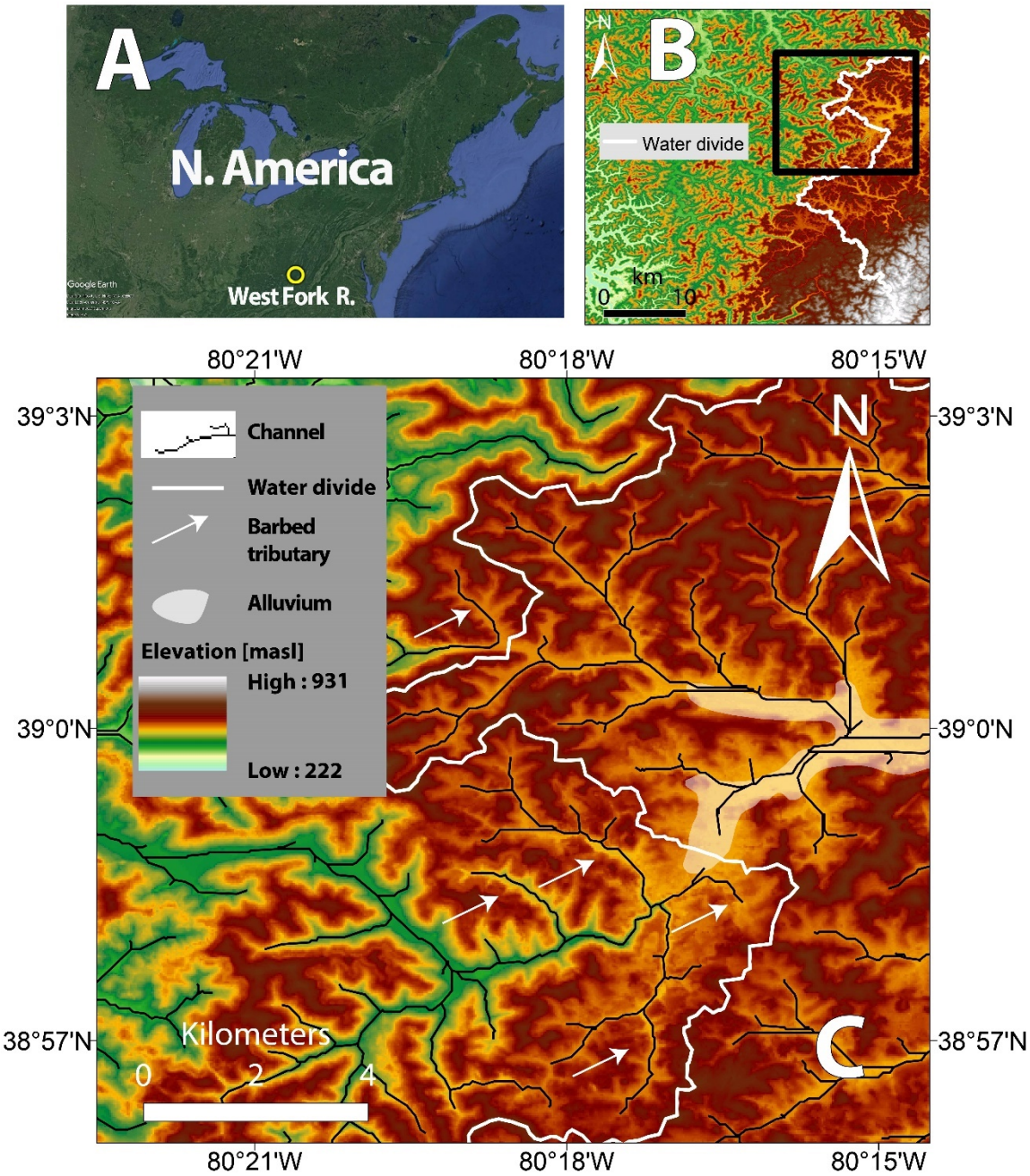

159

160 Figure DR1. Barbed drainages in Fall Run, a tributary of the West Fork river, West
161 Virginia. A. General Location map. B. Zoom-in location map. West to the water divide,
162 steep, west flowing channels incise the highlands. C. Reversed channels with barbed
163 tributaries. Here, the headwater of a reversed channel is incised in a mapped alluvial unit
164 (Cardwell et al., (1968)) that fills the antecedent, east flowing valley.

165

166

(5) FIGURE DR2.

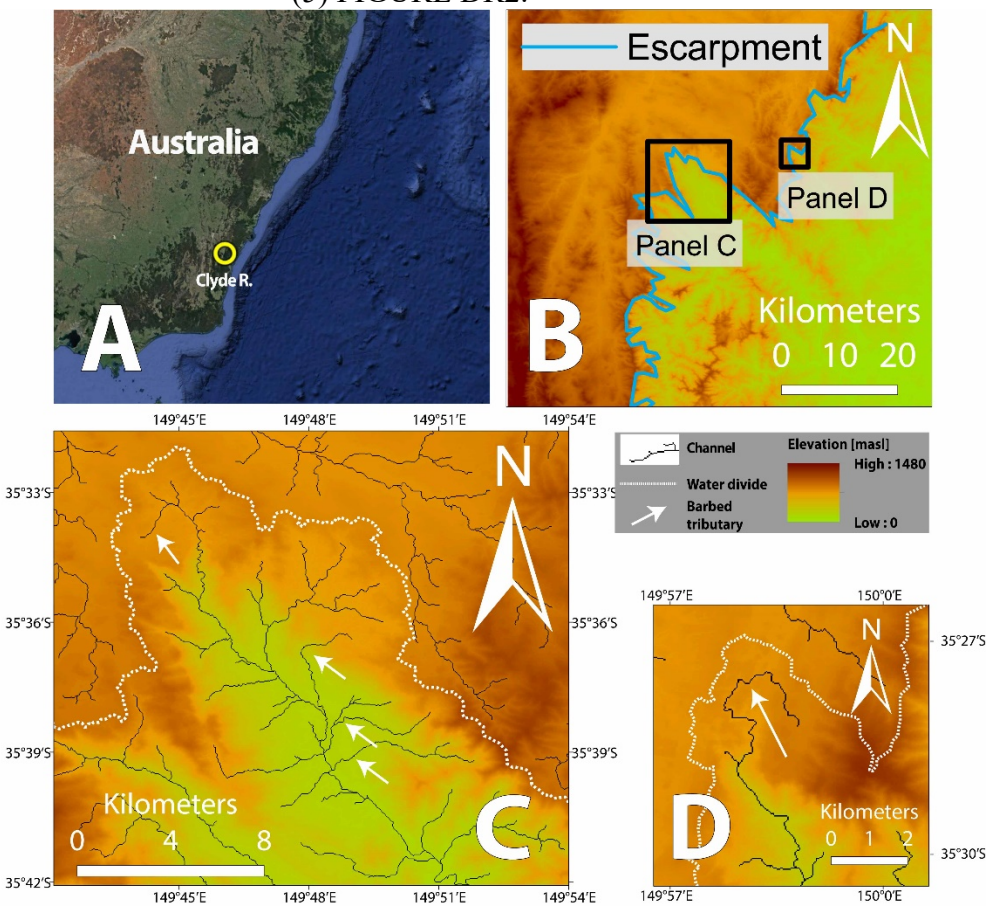

Figure DR2. Barbed drainage morphology in the headwaters of the Clyde river near the great escarpment of eastern Australia. The barbed drainage indicates drainage reversal in the Clyde river. This is a single example out of many along the great escarpment of eastern Australia (Ollier and Pain, 1997; Ollier, 1995; Seidl et al., 1996) A. General Location map. B. Zoom-in location map, depicting the shoulder-type escarpment (i.e. Matmon et al., 2002), and referring to panel C and D. Reversed channels with barbed tributaries in C and hook-shape headwaters in D. Note the embayment of the escarpment along the reversed channels.

178 (6) FIGURE DR3.

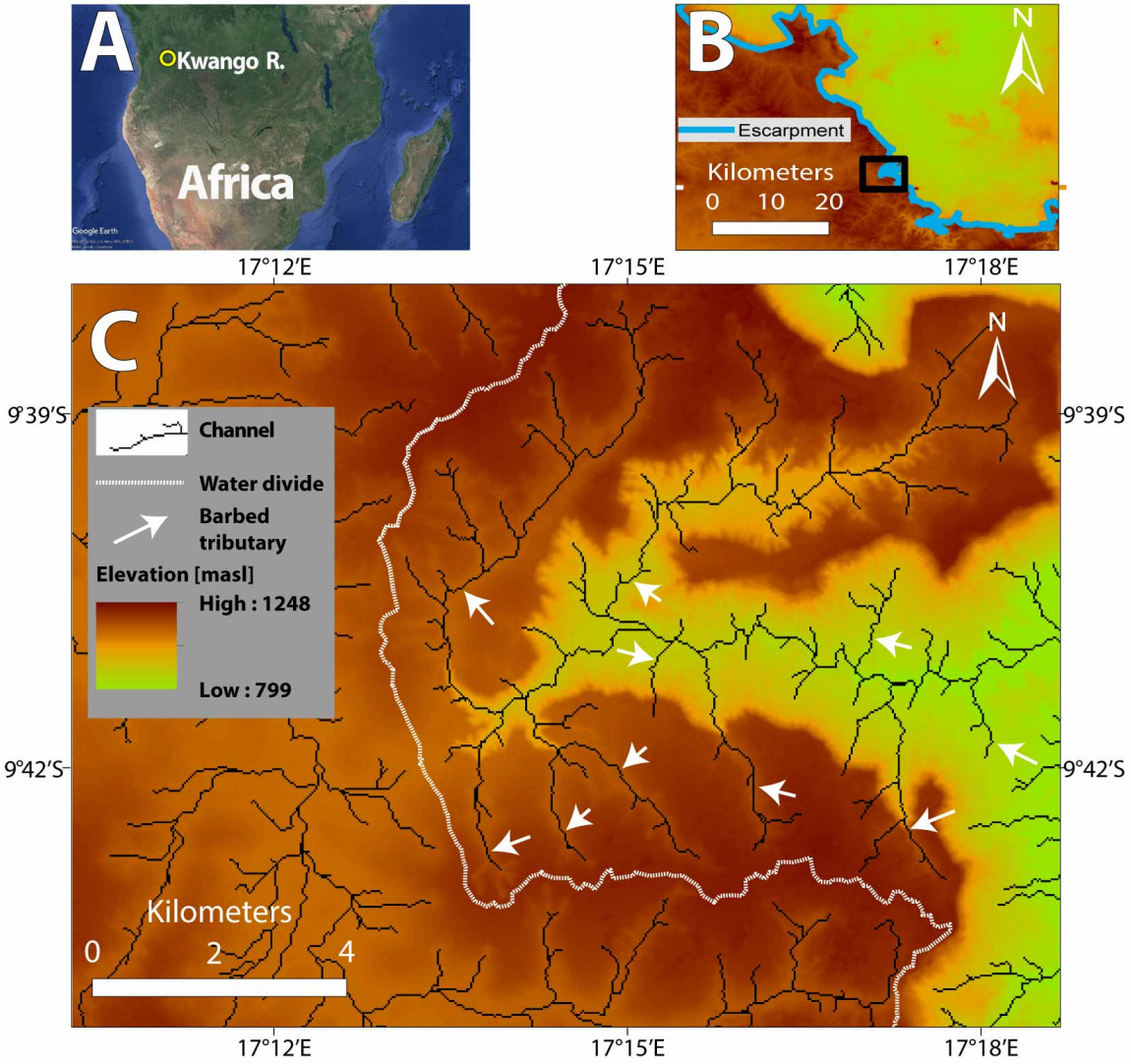

179
180 Figure DR3. Barbed drainage morphology in the headwaters of the Kwango river,
181 Angola, near a shoulder-type escarpment. A. General Location map. B. Zoom-in location
182 map, depicting the escarpment. C. A large basin with barbed tributaries that flow from
183 the highland across the escarpment. Note the extreme embayment of the escarpment,
184 which probably occurs through knickpoint migration along the reversed channel.
185
186

(7) FIGURE DR4.

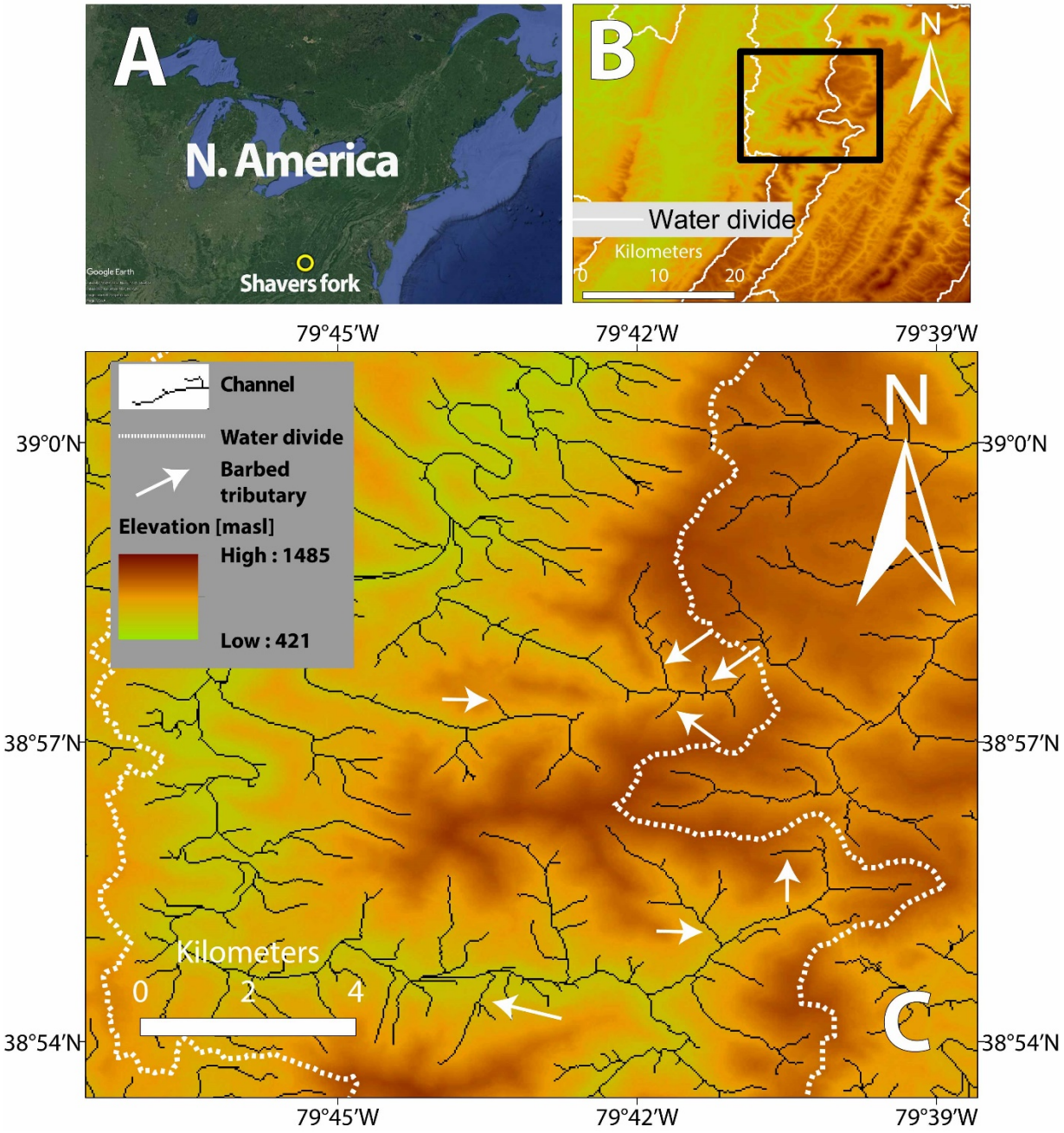

Figure DR4. Barbed drainages in the Shavers fork, near an erosional escarpment in West Virginia. A. General Location map. B. Zoom-in location map. The highland is incised by large channels that drain northward. C. Reversed channels with barbed tributaries drain the highland across the escarpment. Note that in this example, reversal occurs toward an erosional escarpment, which is not part of the Appalachian continental divide.

199 (8) FIGURE DR5.

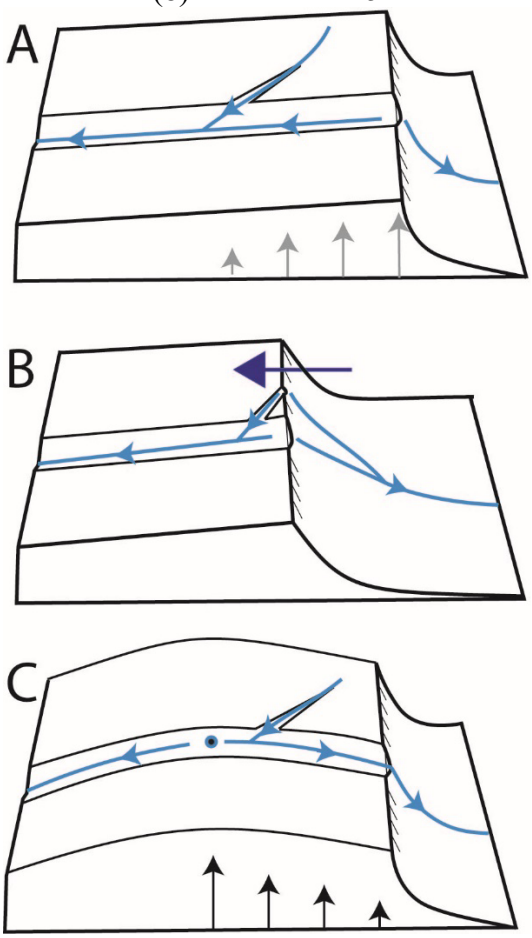

200
201
202 Figure DR5. A cartoon showing the expected effect of tectonic tilting and cliff retreat on
203 diverging channels across a cliff. A. Tilting away from the cliff, depicted by the gray
204 arrows, is predicted by geodynamic models for great escarpments (Gilchrist and
205 Summerfield, 1990; King and Ellis, 1990). Such tilting hinders reversal towards the cliff.
206 B. Simultaneous cliff and divide retreat (blue arrow) erases the antecedent drainage
207 pattern and cannot produce reversed drainages. C. Tectonic tilt toward the cliff (black
208 arrows) could induce flow reversal toward the cliff (Bishop, 1995), but a general source
209 for such a tilt is not recognized.
210
211
212
213
214
215

216 (9) FIGURE DR6.

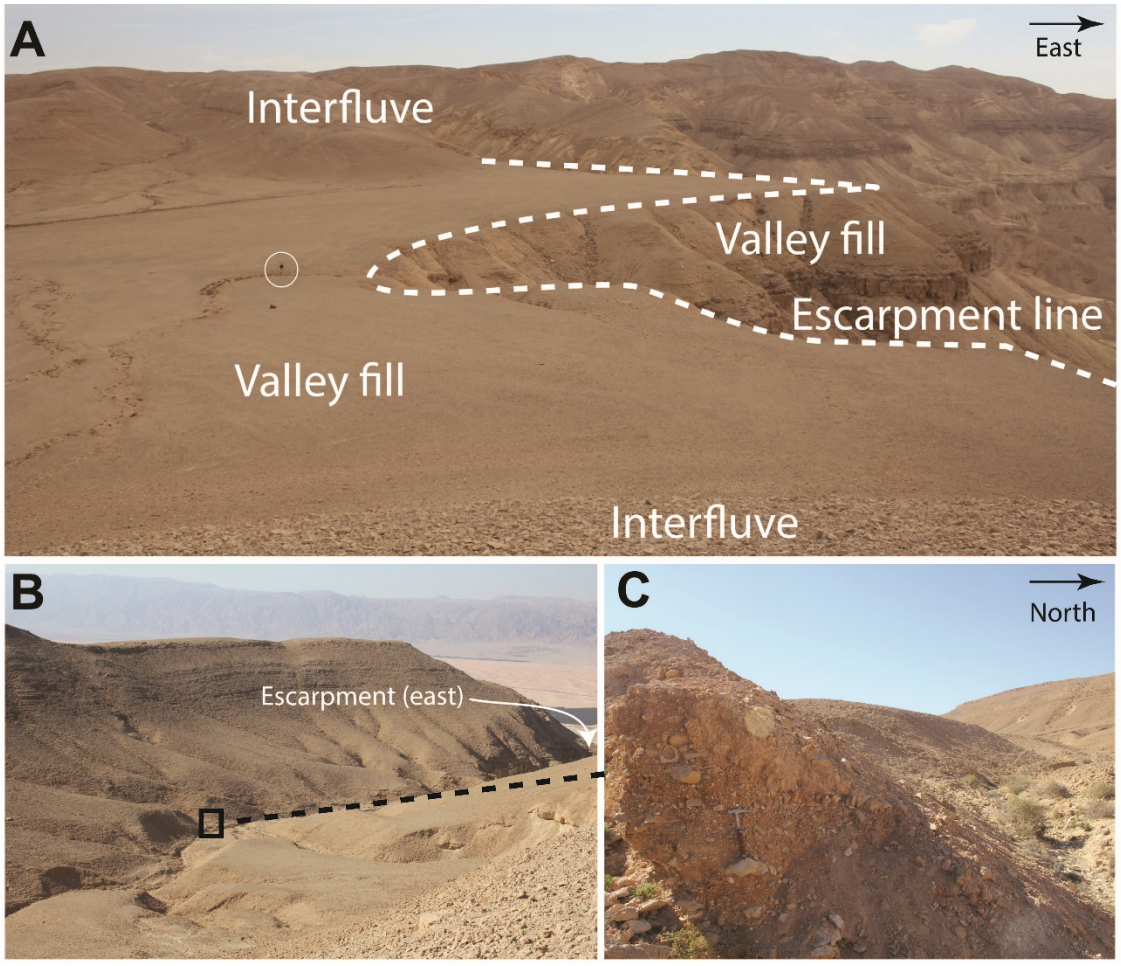

217

218 Figure DR6: Field photos showing two stages in the evolution of reversed channels that
219 flow toward the escarpment. A. View of a wide truncated valley full of sediments (the
220 white circle marks a person's figure for scale), that formed by escarpment retreat. A short
221 reversed channel (no. 36 in the supplementary DR1 table) incises in the erodible fill
222 toward the Arava Valley. B. View of Itro east valley (no. 10 in the supplementary DR1
223 table), that incises into erodible terraces that cover the channel bed. Note the contrast
224 between the hard limestone that caps the interfluves and the more erodible colluvial-
225 alluvial deposits that fill the valley. C. Close-up on a sediment fill outcrop within a
226 terrace in Itro east valley, showing alternating silts and angular small gravel, mixed with
227 colluvial large boulders of up to few tens of cm. Hammer for scale.

228

229 (10) FIGURE DR7.

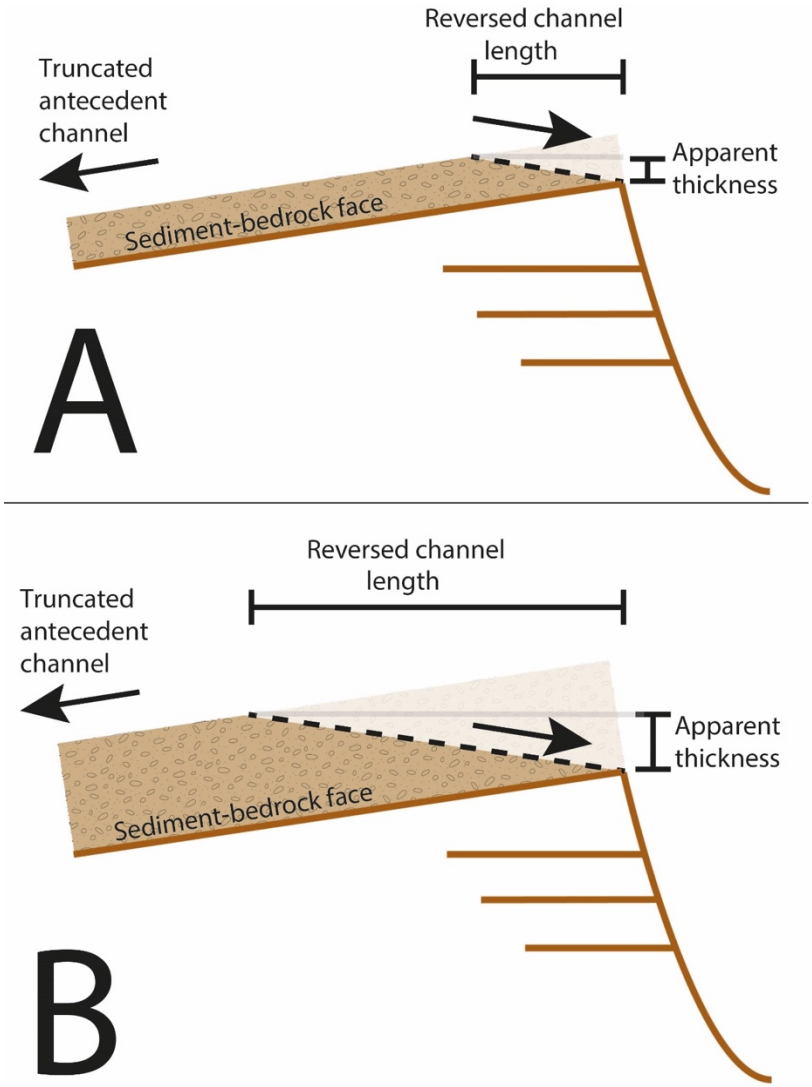

230

231 Figure DR7: A conceptual cartoon showing the expected correlation between the
232 thickness of the erodible fill and the length of the reversed channel segments. The source
233 of the fill can be fluvial, from the antecedent channel, or colluvial from the adjacent
234 hillslopes. The dashed lines represent the course of the reversed segments that incise into
235 the erodible fill, and the transparent grey line is the water divide elevation. The profile of
236 the reversed channels can vary from immature convex to mature concave. Here, for
237 simplicity, it is depicted by a straight dashed line, whose slope is similar in magnitude
238 and opposite in direction to the antecedent channel slope, producing transiently stable
239 divide. A and B for thin and thick erodible fills that produce short and long reversed
240 segments, respectively.

241 (11) FIGURE DR8.

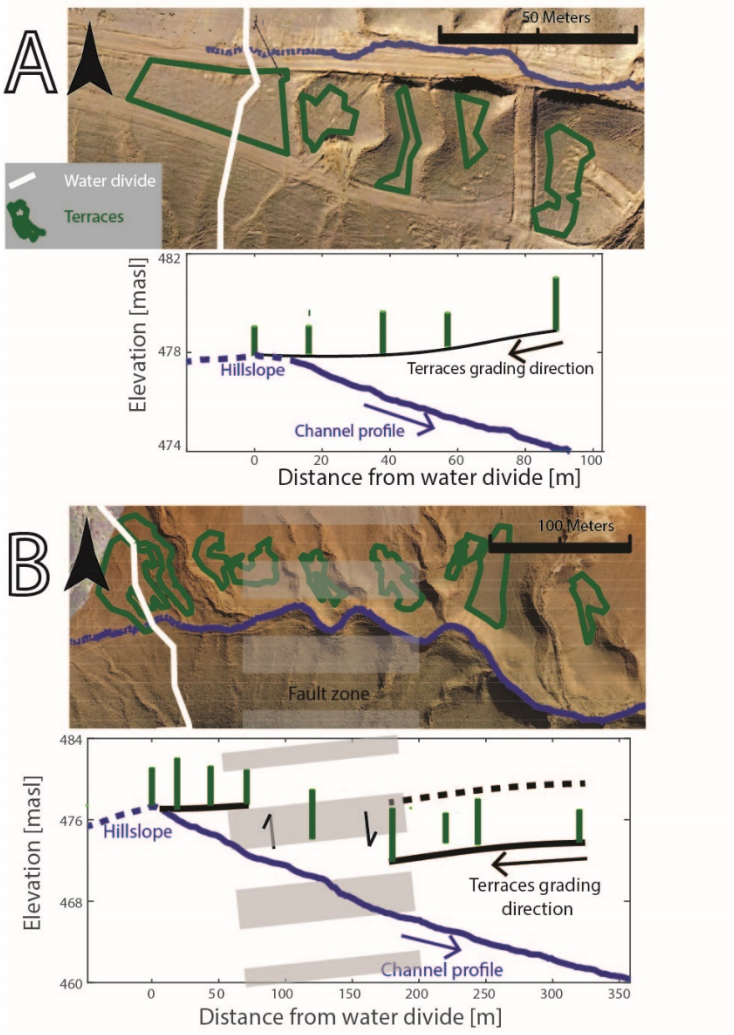

242

243 Fig. DR8. Drone acquired aerial photos of reversed channels showing east flowing
244 channels incised into west grading terraces. In each site, the terraces, the channel route
245 and the divide are shown over the aerial photo (top). The longitudinal profile and the
246 projection of the terraces are shown at the bottom. The green bars indicate the maximum
247 and minimum elevation of each terrace and the black curves show an interpreted surface
248 that grades to the west. A. Upper Shaharut East Basin (see methods DR1). B. An upper
249 reach of Itro East Basin. Here, we mapped a steep fault and propose that it offsets the east
250 group of terraces downward by 5-6 meters with respect to the west terraces. The dashed
251 black line shows the reconstructed elevation of the lower extent of the east terraces prior
252 to faulting.

253 (12) FIGURE DR9.

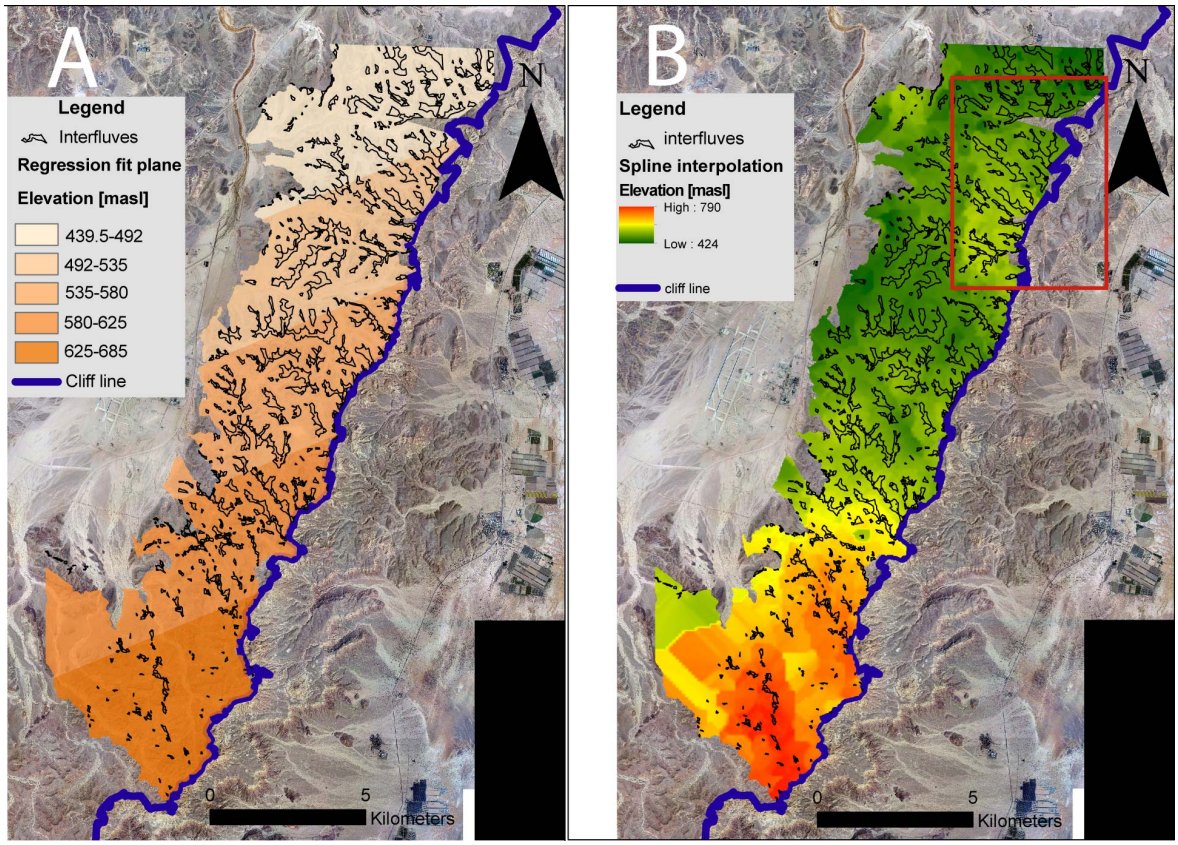

254
255 Figure DR9. A. Linear regression plane based on the elevation of the flat interfluves
256 (small black polygons) in the study area. The interfluves were extracted automatically by
257 identifying low relief surfaces far from channels and were validated by visual inspection.
258 The surface shows highland grading to the northwest, which is not expected to contribute
259 to eastward flow reversal. The blue line marks the escarpment edge, separating the
260 southeastern Negev highland at the west from the Arava Valley at the east. B. Spline
261 interpolation surface, based on the elevation of the flat interfluves in the study area. Note
262 that although the spline surface generally grades to the northwest, small regions along the
263 north part close to the cliff edge (in the red rectangle) show local gradient to the north or
264 northeast.
265

(13) References

Amit, R., Zilberman, E., Enzel, Y., and Porat, N., 2002, Paleoseismic evidence for time dependency of seismic response on a fault system in the southern Arava Valley, Dead Sea rift, Israel: GSA Bulletin, v. 114, p. 192–206, http://dx.doi.org/10.1130/0016-7606(2002)114%3C0192:PEFTDO%3E2.0.CO.

Avni, Y., Bartov, Y., Garfunkel, Z., and Ginat, H., 2000, Evolution of the Paran drainage basin and its relation to the Plio-Pleistocene history of the Arava Rift western margin, Israel.: Israel Journal of Earth Sciences, v. 49, p. 215–238, doi: 10.1560/W8WL-JU3Y-KM7W-8LX4.

Avni, Y., Segev, A., and Ginat, H., 2012, Oligocene regional denudation of the northern Afar dome: Pre- and syn-breakup stages of the Afro-Arabian plate: Bulletin of the Geological Society of America, v. 124, p. 1871–1897, doi: 10.1130/B30634.1.

Beyth, M., Sagy, A., Hajazi, H., Alkhraisha, S., Mushkin, A., and Ginat, H., 2018, New evidence on the accurate displacement along the Arava/Araba segment of the Dead Sea Transform: International Journal of Earth Sciences, v. 107, p. 1431–1443, doi: 10.1007/s00531-017-1549-7.

Bishop, P., 1995, Drainage rearrangement by river capture, beheading and diversion: Progress in Physical Geography, v. 19, p. 449–473, doi: 10.1177/030913339501900402.

Garfunkel, Z., Ben-Avraham, Z., and Kagen, E., 2014, Dead Sea Transform Fault System : Reviews: 183–205 p., doi: 10.1007/978-94-017-8872-4_7.

Gilchrist, A.R., and Summerfield, M.A., 1990, Differential denudation and flexural isostasy in formation of rifted-margin upwarps: Nature, v. 346, p. 739,

289 http://dx.doi.org/10.1038/346739a0.
290 Ginat, H., Enzel, Y., and Avni, Y., 1998, Translocated Plio-Pleistocene drainage systems
291 along the Arava fault of the Dead Sea transform: Tectonophysics, v. 284, p. 151–
292 160, doi: 10.1016/S0040-1951(97)00165-0.
293 Ginat, H., Zilberman, E., and Avni, Y., 2000, Tectonic and paleogeographic significance
294 of the Edom River , a Pliocene stream that crossed the Dead Sea Rift valley: Israel
295 Journal of Earth Sciences, v. 49, p. 159–177, doi: 10.1560/N2P9-YBJ0-Q44Y-
296 GWYN.
297 Guralnik, B., Matmon, A., Avni, Y., and Fink, D., 2010, 10Be exposure ages of ancient
298 desert pavements reveal Quaternary evolution of the Dead Sea drainage basin and
299 rift margin tilting: Earth and Planetary Science Letters, v. 290, p. 132–141, doi:
300 10.1016/j.epsl.2009.12.012.
301 King, G., and Ellis, M., 1990, The origin of large local uplift in extensional regions:
302 Nature, v. 348, p. 689, http://dx.doi.org/10.1038/348689a0.
303 Mart, Y., and Vachtman, D., 2015, The internal grabens of the Levant Rifts and their
304 geodynamic significance: Comptes Rendus Geoscience, v. 347, p. 191–200, doi:
305 10.1016/j.crte.2015.06.010.
306 Matmon, A., Bierman, P., and Enzel, Y., 2002, Pattern and tempo of great escarpment
307 erosion: Geology, v. 30, p. 1135–1138, http://dx.doi.org/10.1130/0091-
308 7613(2002)030%3C1135:PATOGE%3E2.0.CO.
309 Ollier, C.D., 1995, Tectonics and landscape evolution in southeast Australia:
310 Geomorphology, v. 12, p. 37–44, doi: https://doi.org/10.1016/0169-555X(94)00075-
311 3.

Ollier, C.D., and Pain, C.F., 1997, Equating the basal unconformity with the palaeoplain: a model for passive margins: Geomorphology, v. 19, p. 1–15, doi: https://doi.org/10.1016/S0169-555X(96)00048-7.

Perron, J.T., and Royden, L., 2012, An integral approach to bedrock river profile analysis: Earth Surface Processes and Landforms, v. 38, p. 570–576.

Seidl, M.A., Weissel, J.K., and Pratson, L.F., 1996, The kinematics and pattern of escarpment retreat across the rifted continental margin of SE Australia: Basin Research, v. 8, p. 301–316.

Vaks, A., Woodhead, J., Bar-Matthews, M., Ayalon, A., Cliff, R.A., Zilberman, T., Matthews, A., and Frumkin, A., 2013, Pliocene–Pleistocene climate of the northern margin of Saharan–Arabian Desert recorded in speleothems from the Negev Desert, Israel: Earth and Planetary Science Letters, v. 368, p. 88–100, doi: https://doi.org/10.1016/j.epsl.2013.02.027.

Wdowinski, S., and Zilberman, E., 1996, Kinematic modelling of large-scale structural asymmetry across the Dead Sea Rift: Tectonophysics, v. 266, p. 187–201, doi: 10.1016/s0040-1951(96)00238-7.

Wdowinski, S., and Zilberman, E., 1997, Systematic analyses of the large-scale topography and structure across the Dead Sea Rift: Tectonics, v. 16, p. 409–424, doi: 10.1029/97TC00814.

Wessel, B., 2016, TanDEM-X Ground Segment – DEM Products Specification Document: EOC, DLR, Oberpfaffenhofen, Germany, Public Document TD-GS-PS-0021, Issue 3.1, https://tandemx-science.dlr.de/.

Willett, S.D., McCoy, S.W., Perron, J.T., Goren, L., and Chen, C.-Y., 2014, Dynamic

reorganization of river basins: Science, v. 343, p. 1248765.